Optimal Design of DCM *LCC* Resonant Converter With Inductive Filter Based on Mode Boundary Map

Xing Tan, *Student Member, IEEE*, and Xinbo Ruan, *Senior Member, IEEE*

***Abstract*—*LCC* resonant converter with inductive filter operating in discontinuous current mode (DCM) can achieve zero-current switching (ZCS) for both the power switches and rectifier diodes. Therefore, it is suitable for high-power, low-voltage, high-current power supplies. The DCM *LCC* resonant converter with inductive filter might operate in different operating modes when input voltage or load changes, which challenges the design. This paper derives a mode boundary map, from which the operating mode of the converter can be easily determined. Based on the mode boundary map, a generalized optimal design procedure is proposed and a set of optimal and normalized converter parameters is determined, which can be easily converted into real parameters according to the converter specification. Three 5 kW prototypes with different converter parameters are fabricated and tested in the lab, and the experimental results show that with the set of optimal parameters, the converter can achieve the highest efficiency over the entire input voltage and load range.**

***Index Terms*—Discontinuous current mode (DCM), *LCC* resonant converter, mode boundary map, optimal design, zero-current switching (ZCS).**

NOMENCLATURE

C_f	Output filter capacitor.
C'_p	Parallel resonant capacitor.
C_p	C'_p that is reflected to the transformer primary side, $C_{\mathrm{p}} = 4C'_p/n^2$.
C_r	Equivalent resonant capacitor, $C_r = C_s C_p/(C_s + C_p)$.
C_s	Series resonant capacitor.
f_r	Resonant frequency, $f_r = 1/\left(2\pi\sqrt{L_r C_r}\right)$.
f_s	Switching frequency.
$f_{s\_\max}$	The maximum switching frequency.
f_{sN}	Normalized form of f_s, $f_{sN} = f_s/f_r$.
i_{Lr}	Current through L_r.
$i_{Lr\mathrm{N}}$	Normalized form of i_{Lr}, $i_{Lr\mathrm{N}} = i_{Lr} Z_{\mathrm{r}}/V_{\mathrm{in}}$.
$I_{L_r\_\mathrm{rms}}$	RMS value of i_{Lr}.
I_{Lr_pk}	Peak value of i_{L_r}.
$I_{Lr\mathrm{N}k}$	Abbreviation of $i_{Lr\mathrm{N}}(\alpha_{\mathrm{k}})$ ($k = 1, 2, 3$).
$I_{Lr\mathrm{N}\_\mathrm{rms}}$	RMS value of $i_{Lr\mathrm{N}}$.
$I_{Lr\mathrm{N}\_\mathrm{pk}}$	Peak value of $i_{L_r\mathrm{N}}$.
$I^*{}_{Lr\_\mathrm{rms}}$	Normalized I_{Lr_rms} with respect to $I_{o\_\max}V_o/V_{\mathrm{in\_min}}$.
$I^*_{Lr\_\mathrm{pk}}$	Normalized I_{Lr_pk} with respect to $I_{o\_\max}V_o/V_{\mathrm{in\_min}}$.
I_o	Output current.
$I_{o\_\max}$	Output current at full load.
I_{oN}	Normalized form of I_o/n, $I_{oN} = I_o Z_r/(nV_{\mathrm{in}})$.
L_f	Output filter inductor.
L_r	Sum of the resonant inductor and the leakage inductor of the transformer.
n	Primary to secondary turns ratio of the transformer.
R_{Ld}	Load resistor.
t_{i+}	Time instant when i_{Lr} crosses zero in the positive directions.
t_{i-}	Time instant when i_{Lr} crosses zero in the negative directions.
t_{v+}	Time instant when v_{C_p} crosses zero in the positive direction.
T_r	Resonant period, $T_r = 1/f_r$.
T_s	Switching period, $T_s = 1/f_s$.
v_{Cs}	Voltage across C_s.
v_{C_p}	Voltage across C_p.
$v_{C'p}$	Voltage across C'_p
$v_{Cs\mathrm{N}}$	Normalized form of v_{Cs}, $v_{Cs\mathrm{N}} = v_{Cs}/V_{\mathrm{in}}$.
$v_{C_p\mathrm{N}}$	Normalized form of v_{C_p}, $v_{C_p\mathrm{N}} = v_{C_p}/V_{\mathrm{in}}$
V'_{Cp_pk}	Peak value of v'_{C_p}.
$V_{C_p\mathrm{N}\_\mathrm{pk}}$	Peak value of $v_{C_p\mathrm{N}}$.
$V_{C_s\mathrm{N}0}$	Abbreviation of $v_{C_s\mathrm{N}}(0)$.
$V_{C_s\mathrm{N}k}$	Abbreviation of $v_{C_s\mathrm{N}}(\alpha_{\mathrm{k}})$, where $k = 1, 2, 3$.
$V_{C_p\mathrm{N}k}$	Abbreviation of $v_{C_p\mathrm{N}}(\alpha_{\mathrm{k}})$, where $k = 1, 2, 3$.
V_{in}	Input voltage.
$V_{\mathrm{in\_min}}$	Minimum input voltage.
$V_{\mathrm{in\_max}}$	Maximum input voltage.
V_o	Output voltage.
V_{oN}	Normalized form of nV_o, $V_{oN} = nV_o/V_{\mathrm{in}}$.
$V^*_{Cp\_\mathrm{pk}}$	Normalized V'_{Cp_pk} with respect to V_o, $V^*_{Cp\_\mathrm{pk}} = V'_{Cp\_\mathrm{pk}}/V_{\mathrm{o}}$.
Z_r	Characteristic impedance of the resonant tank, $Z_r = \sqrt{L_r/C_r}$.
α	Normalized form of time t, $\alpha = \omega_r t$.
α_{12}	Abbreviation of $\alpha_2 - \alpha_1$.
α_{23}	Abbreviation of $\alpha_3 - \alpha_2$.
α_k	Normalized form of t_k ($k = 0, 1, 2, 3$).

Manuscript received April 29, 2014; revised August 2, 2014; accepted September 7, 2014. Date of publication September 24, 2014; date of current version March 5, 2015. Recommended for publication by Associate Editor T. Qian.

X. Tan is with the State Key Laboratory of Advanced Electromagnetic Engineering and Technology, Huazhong University of Science and Technology, Wuhan 430074, China (e-mail: tanxing@hust.edu.cn).

X. Ruan is with the State Key Laboratory of Advanced Electromagnetic Engineering and Technology, Huazhong University of Science and Technology, Wuhan 430074, China, and also with the Aero-Power Sci-Tech Center, College of Automation Engineering, Nanjing University of Aeronautics and Astronautics, Nanjing 210016, China (e-mail: ruanxb@ hust.edu.cn).

Color versions of one or more of the figures in this paper are available online at http://ieeexplore.ieee.org.

Digital Object Identifier 10.1109/TPEL.2014.2360127

λ Capacitor ratio, $\lambda = C_p/C_s$.
ω_r Resonant angular frequency, $\omega_r = 2\pi f_r$.

I. INTRODUCTION

High-power, low-voltage, high-current power supplies are widely used in electroplating [1], electrolyzing [2], welding [3] and excitation for superconducting magnet [4], etc. In these power supplies, IGBTs are commonly employed as the power switches. It is preferred to achieve zero-current switching (ZCS) for IGBTs to reduce the turn-off losses resulted by the current tail [5].

Resonant converters are good candidates for achieving ZCS. Series resonant converter (SRC) [6] and parallel resonant converter (PRC) [7] are two basic resonant converters. SRC offers high efficiency at light load, but it has a wide range of switching frequency and its output voltage cannot be regulated at no load [8]. PRC has a narrow range of switching frequency, and its output voltage can be regulated at no load; however, the efficiency at light load is relatively low [8]. In order to overcome the disadvantages of SRC and PRC, various other resonant converters with more than two resonant components have been proposed [9], [10]. Among them, *LLC* resonant converter [11], [12] and *LCC* resonant converter [13]–[24] are the most popular converters.

The output filter of a resonant converter can be either a capacitive filter or an inductive filter [9], [10]. For the *LLC* resonant converter, the output filter should be the capacitive one. For the *LCC* resonant converter, both the capacitive filter [13]–[19] and inductive filter [20]–[24] can be adopted. In high-power, low-voltage, high-current power supplies, the inductive filter is attractive since the current ripple in the output filter capacitor is relatively smaller compared to that in the capacitive filter. Therefore, *LCC* resonant converter with inductive filter is attractive for these applications.

The *LCC* resonant converter with inductive filter can operate in continuous current mode (CCM) [20]–[22] or discontinuous current mode (DCM) [23], [24]. In CCM, if the *LCC* resonant converter with inductive filter operates above resonance, the power switches can achieve zero-voltage switching (ZVS) [20], [21]; if it operates below resonance, the power switches can achieve ZCS turn-off, but hard turn-on [22]. In DCM, both the ZCS turn-on and turn-off can be achieved, leading to low switching losses [23], [24]. Therefore, letting the *LCC* resonant converter with inductive filter to operate in DCM is a better choice for high-power, low-voltage, high-current applications.

The design of *LCC* resonant converter has been extensively discussed [13]–[24], and the DCM *LCC* resonant converter with inductive filter has been focused on in [23] and [24]. The DCM *LCC* resonant converter with inductive filter can operate in various operating modes, and the operating mode might change with the variations of input voltage and load, which challenges the design of the converter parameters. In [23] and [24], two different operating modes are considered for design, respectively, and therefore, the converter has not been optimized with variations of the input voltage and load. What's more, these designs are based on the specific specifications of the converters. For different specifications, the converter should be redesigned. To solve these problems, this paper proposes the concept of the mode boundary map for the DCM *LCC* resonant converter with inductive filter, from which the operating mode of the converter can be easily determined. Based on the mode boundary map, a generalized optimal design procedure with the variations of input voltage and load is proposed and a set of normalized converter parameters is determined, which can be easily converted into real converter parameters, no matter what the converter specification is. With this set of parameters, the converter can achieve a high efficiency over the entire input voltage and load ranges.

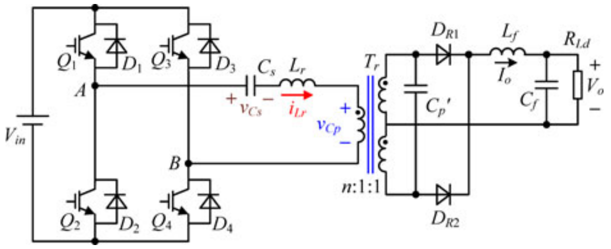

Fig. 1. Main circuit of the *LCC* resonant converter with inductive filter.

This paper is organized as follows. In Section II, the possible operating modes of the DCM *LCC* resonant converter with inductive filter are briefly reviewed. In Section III, the mode boundary map is derived. In Section IV, the steady-state characteristics of the converter are given. In Section V, a set of optimal and normalized converter parameters is determined based on the mode boundary map. In Section VI, three 50 V/100 A prototypes are fabricated and tested. One prototype is designed with the proposed set of optimal parameters, the other two prototypes are used for comparisons. In these two prototypes, one is designed with the set of parameters from [24], and the other is designed with the parameters so that it acts as a DCM PRC. The experimental results verify that the prototype with the proposed set of parameters achieves a higher efficiency than the other two prototypes over the entire input voltage and load range. Finally, Section VII concludes this paper.

II. REVIEW OF OPERATING MODES OF DCM *LCC* RESONANT CONVERTER WITH INDUCTIVE FILTER

Fig. 1 shows the main circuit of the *LCC* resonant converter with inductive filter. The parallel resonant capacitor C_p' is intentionally placed on the secondary side of the transformer to make use of the leakage inductor of the transformer as a part of the resonant inductor. The inductor L_r represents the sum of the resonant inductor and the leakage inductor of the transformer. L_f and C_f form the inductive filter. The converter is operated in DCM by gating the switches $Q_1 - Q_4$ with a fixed on-time and variable frequency to regulate the output voltage.

Before analysis, it is assumed that all the components are ideal and L_f is large enough to be regarded as a current source with the value of output current I_o. Due to the symmetrical operation, only the half cycle when Q_1 and Q_4 are conducting is analyzed here. Fig. 2 shows all the possible equivalent circuits

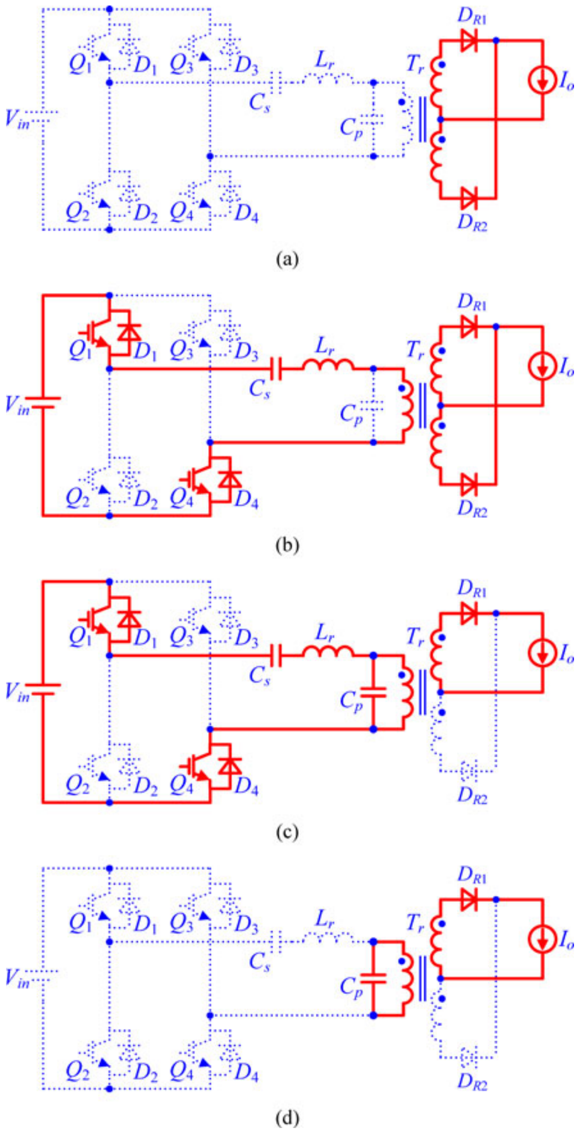

(a) (b) (c) (d)

Fig. 2. Possible operating intervals in half cycle. (a) Interval 0. (b) Interval 1. (c) Interval 2. (d) Interval 3.

during different operating intervals in half cycle, where the circuit formed by L_f, C_f, and R_{Ld} is simplified to the current source I_o and the parallel resonant capacitor C_p' is reflected to the primary side of the transformer, denoted by C_p.

Interval 0 [Prior to 0]: $i_{L_r} = 0$ and the load current I_o freewheels through D_{R1} and D_{R2}. Therefore, $v_{C_p} = 0$ and v_{Cs} has an initial value.

Interval 1 [t_0, t_1]: At t_0, Q_1, and Q_4 are turned on with ZCS, and V_{in} is applied on the resonant tank. Consequently, L_r and C_s start to resonate, and i_{L_r} increases from zero. As $i_{L_r} < I_{\mathrm{o}}/n$, D_{R1} and D_{R2} still keep conducting and $v_{C_p} = 0$.

Interval 2 [After t_1]: At t_1, i_{L_r} increases to I_o/n. D_{R2} turns off naturally, and I_o flows through D_{R1}. After t_1, $i_{L_r} > I_{\mathrm{o}}/n$. Hence, C_p is charged and v_{C_p} increases from zero. L_r, C_s, and C_p start to resonate.

In the course of resonance, i_{L_r} will cross zero twice: the first time is that i_{L_r} crosses zero from the positive direction, denoted by t_{i+}; and the second time is that i_{L_r} crosses zero from the negative direction, denoted by t_{i-}. v_{Cp} will cross zero once from the positive direction, denoted by t_{v+}. t_{v+} could be later than t_{i-}, within [t_{i+}, t_{i-}], or earlier than t_{i+}, and this will lead to three possible operating modes, which are named as Mode 1, Mode 2, and Mode 3, respectively. The key operating waveforms of these three operating modes are shown in Fig. 3. In these operating modes, Q_1 and Q_4 are turned off with

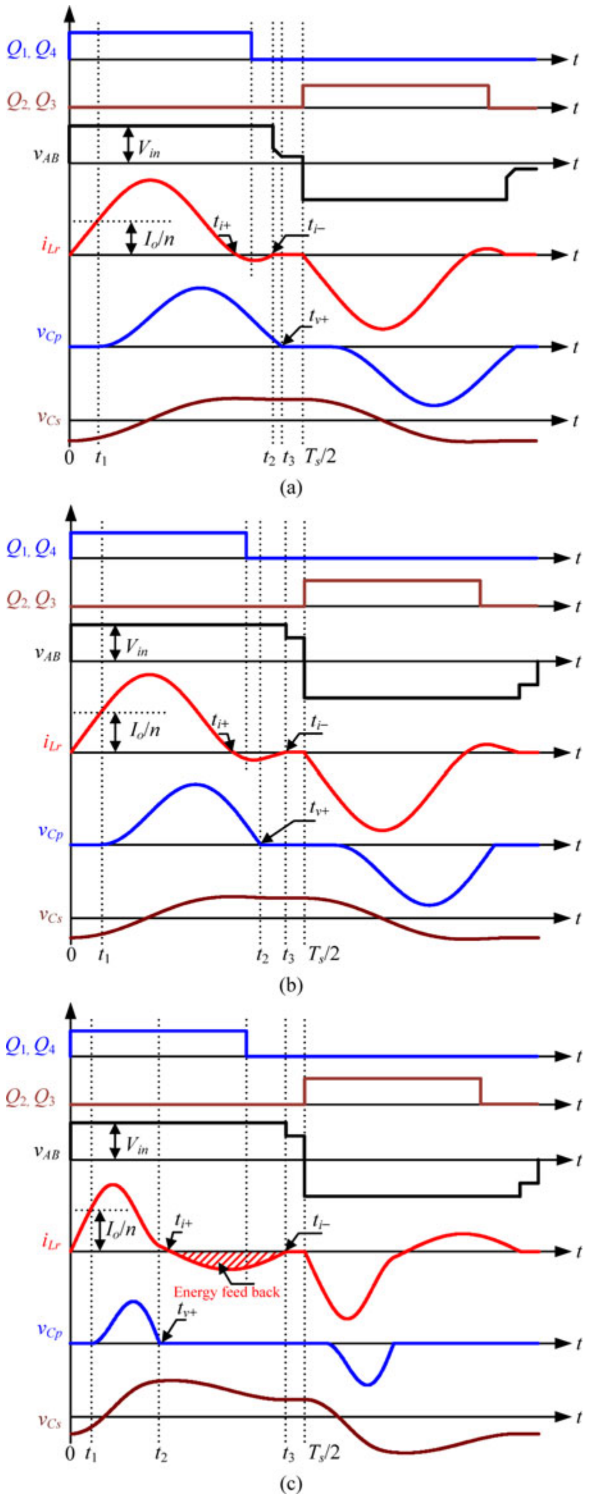

(a) (b) (c)

Fig. 3. Key operating waveforms. (a) Mode 1. (b) Mode 2. (c) Mode 3.

TABLE I
DEFINITION OF BASE QUANTITIES

Voltage	Impedance	Current	Time	Frequency
V_{in}	Z_r	V_{in}/Z_r	$1/\omega_r$	f_r

ZCS when i_{L_r} declines to negative and flows through D_1 and D_4 during $[t_{i+}, t_{i-}]$. When both i_{L_r} and v_{Cp} return to zero, the converter will return to Interval 0. The detailed equations of Mode 1 and Mode 2 can be found from [23] and [24], respectively. The normalized forms of the equations of all these three operating modes are derived in Appendix A. The physical quantities in these equations are normalized with respect to the base quantities defined in Table I. Steady-state solutions of the converter can be obtained from these equations.

III. DERIVATION OF THE MODE BOUNDARY MAP

A. Boundary Curve Between Mode 1 and Non-ZCS Area

As seen in Fig. 3(a), L_r C_s and C_p resonate after t_1 in Mode 1. In order to achieve ZCS turn-off for the power switches, i_{L_r} should cross zero. So, according to (A8), we have

$$\frac{I_{o\text{N}}}{1+\lambda} \leq \sqrt{\left(\frac{\lambda I_{o\text{N}}}{1+\lambda}\right)^2 + (1 - V_{C_s\text{N}1})^2}. \tag{1}$$

According to (1), the boundary condition between Mode 1 and non-ZCS area is

$$\frac{I_{o\text{N}}}{1+\lambda} = \sqrt{\left(\frac{\lambda I_{o\text{N}}}{1+\lambda}\right)^2 + (1 - V_{C_s\text{N}1})^2}. \tag{2}$$

Combining and solving (2), (A5), (A9), (A11), and (A16) can obtain the equation of the boundary curve of Mode 1 and non-ZCS area as

$$I_{o\text{N}} = \frac{2}{\dfrac{1+(1-\lambda)^{3/2}}{\sqrt{1+\lambda}} - \dfrac{\lambda(1.5\pi - \arcsin\lambda - \lambda\sqrt{1-\lambda^2})}{(1+\lambda)^2}} \tag{3}$$

where $I_{oN} = I_o Z_r/(nV_{\text{in}})$, $\lambda = C_p/C_s$. The detailed derivation of (3) is shown in Appendix B. According to (3), Curve 1, which is the boundary curve between Mode 1 and non-ZCS area is drawn in Fig. 4.

B. Boundary Curve Between Mode 1 and Mode 2

$t_{v+} = t_{i-}$ is the boundary condition between Mode 1 and Mode 2. This implies $V_{Cp\text{N}2} = 0$ in Mode 1. Likewise, combining and solving $V_{Cp\text{N}2} = 0$, (A5), (A9)–(A11), and (A16), the boundary curve equation between Mode 1 and Mode 2 can be derived as

$$\begin{cases} \tan\left(\dfrac{\alpha_{12}}{2}\right) + \dfrac{\lambda\alpha_{12}}{1-\lambda} = 0 \\ I_{o\text{N}} = \sqrt{\left(\dfrac{1-\lambda^2-\lambda^2\alpha_{12}^2}{\lambda\alpha_{12}}\right)^2 + 4(1+\lambda)} - \dfrac{1-\lambda^2-\lambda^2\alpha_{12}^2}{\lambda\alpha_{12}}. \end{cases} \tag{4}$$

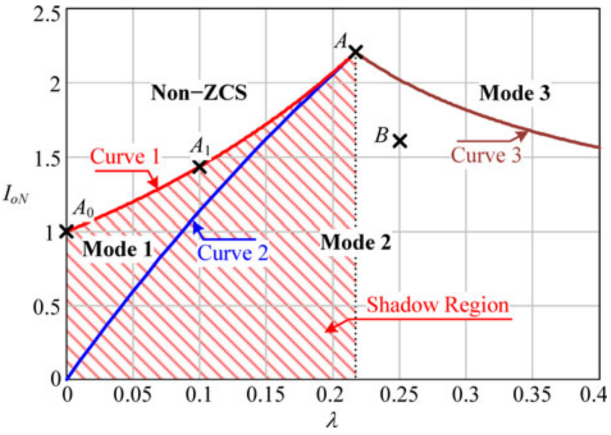

Fig. 4. Mode boundary map of DCM *LCC* resonant converter with inductive filter.

According to (4), Curve 2, which is the boundary curve between Mode 1 and Mode 2, is drawn in Fig. 4.

C. Boundary Curve Between Mode 2 and Mode 3

$t_{v+} = t_{i+}$ is the boundary condition between Mode 2 and Mode 3. This implies $I_{Lr\text{N}2} = 0$ in Mode 2. Likewise, solving $I_{Lr\text{N}2} = 0$, (A5), (A17)–(A19), (A23), (A24), and (A25), the equation of the boundary curve between Mode 2 and Mode 3 can be derived as

$$\begin{cases} \tan(\alpha_{12}/2) + \lambda\alpha_{12}/(1-\lambda) = 0 \\ I_{o\text{N}} = \sqrt{\left(\dfrac{1-\lambda^2-\lambda^2\alpha_{12}^2}{\lambda\alpha_{12}}\right)^2 + 4(1+\lambda)} + \dfrac{1-\lambda^2-\lambda^2\alpha_{12}^2}{\lambda\alpha_{12}} \end{cases}. \tag{5}$$

According to (5), Curve 3, which is the boundary curve between Mode 2 and Mode 3, is drawn in Fig. 4.

Since Curve 1 is the boundary curve between Mode 1 and non-ZCS area, it has $t_{i+} = t_{i-}$ on Curve 1. Likewise, on Curve 2, $t_{v+} = t_{i-}$. Therefore, at the intersection point A of Curve 1 and Curve 2, $t_{v+} = t_{i+}$, which is the condition of Curve 3. So Curve 3 also crosses point A. That means Curve 1, Curve 2, and Curve 3 intersect at the point A. By solving (3) and (4), we have $\lambda = 0.217$, $I_{o\text{N}} = 2.209$ at point A.

IV. STEADY-STATE CHARACTERISTICS OF THE CONVERTER

In this section, the steady-state characteristics of the converter include voltage gain and component stresses will be analyzed to facilitate the optimal design.

A. Voltage Gain

The voltage gain of the converter is defined as $V_{o\text{N}} = nV_o/V_{\text{in}}$. As seen in Fig. 1, $V_{o\text{N}}$ equals to the average value of $v_{Cp\text{N}}$ during $[t_0, T_s/2]$. Therefore, referring to Fig. 3, $V_{o\text{N}}$ can be expressed as

$$V_{o\text{N}} = \frac{f_{s\text{N}}}{\pi} \int_{\alpha_1}^{\alpha_3} v_{C_p\text{N}}(\alpha)\,d\alpha \tag{6}$$

where the expression of $v_{C_p\mathrm{N}}(\alpha)$ is (A7) when $\alpha_1 \le \alpha \le \alpha_2$; and when $\alpha_2 \le \alpha \le \alpha_3$, the expression of $v_{C_p\mathrm{N}}(\alpha)$ is (A13) for Mode 1, and $v_{C_p\mathrm{N}}(\alpha) = 0$ for Mode 2 and Mode 3.

According to Appendix C, in Mode 1 and Mode 2, the approximate expression of $V_{o\mathrm{N}}$ can be obtained as

$$V_{o\mathrm{N}} \approx \frac{2f_{s\mathrm{N}}}{1+\lambda}. \tag{7}$$

In DCM, the maximum switching frequency is about the half of the resonant frequency f_r, which indicates the maximum $f_{s\mathrm{N}}$ is about 0.5. Substituting $f_{s\mathrm{N}} = 0.5$ into (7) gives that the maximum $V_{o\mathrm{N}}$ is about $1/(1+\lambda)$. That means the voltage gain $V_{o\mathrm{N}}$ is always smaller than 1. It can also be known from (7) that when switching frequency and input voltage are constant, the output voltage will be constant and is independent of the load.

B. *Component Stresses*

Referring to Fig. 3, the rms value of $i_{L_r\mathrm{N}}$ is expressed as

$$I_{L_r\mathrm{N\_rms}} = \sqrt{\frac{f_{s\mathrm{N}}}{\pi}\int_0^{\alpha_3} i^2_{L_r\mathrm{N}}(\alpha)d\alpha} \tag{8}$$

where the expressions of $i_{L_r\mathrm{N}}(\alpha)$ are (A3) and (A8) when $0 \le \alpha \le \alpha_1$ and $\alpha_1 \le \alpha \le \alpha_2$ respectively; and when $\alpha_2 \le \alpha \le \alpha_3$, $i_{L_r\mathrm{N}}(\alpha)$ is zero for Mode 1, and $i_{L_r\mathrm{N}}(\alpha)$ is expressed as (A22) for Mode 2 and Mode 3.

As seen in Fig. 3, $i_{L_r\mathrm{N}}$ reaches its peak value $I_{L_r\mathrm{N\_pk}}$ during $[t_1, t_2]$. From (A8), we have

$$I_{L_r\mathrm{N\_pk}} = \frac{I_{o\mathrm{N}}}{1+\lambda} + \sqrt{\left(\frac{\lambda I_{o\mathrm{N}}}{1+\lambda}\right)^2 + (1 - V_{C_s\mathrm{N}1})^2}. \tag{9}$$

Again, as seen in Fig. 3, $v_{C_p\mathrm{N}}$ reaches its peak value when $i_{L_r} = I_o/n$ during $[t_1, t_2]$. From (A7) and (A8), we have

$$V_{C_p\mathrm{N\_pk}} = \frac{2}{1+\lambda}\left[1 - V_{C_s\mathrm{N}1} - \frac{\lambda I_{o\mathrm{N}}}{1+\lambda}\arctan\frac{(1+\lambda)(1 - V_{C_s\mathrm{N}1})}{\lambda I_{o\mathrm{N}}}\right]. \tag{10}$$

V. OPTIMAL DESIGN OF CONVERTER PARAMETERS BASED ON THE MODE BOUNDARY MAP

In this section, a generalized optimal design will be implemented based on the mode boundary map to achieve a high efficiency over the entire input voltage and load range. As the design is based on normalized values, it is not necessary to know the specific values of the converter specification, and only the symbols of the specification are listed below:

1) Input voltage: $V_{\mathrm{in\_min}}$–$V_{\mathrm{in\_max}}$;
2) Output voltage: V_o;
3) Output current at full load: $I_{o\_\max}$;
4) Maximum switching frequency: $f_{s\_\max}$.

As seen from (7), $V_{o\mathrm{N}}$ is proportional to $f_{s\mathrm{N}}$ and is independent of $I_{o\mathrm{N}}$. That means the switching frequency doesn't vary with load and the variation range of switching frequency is proportional to the variation range of input voltage. Therefore, the range of switching frequency can not be reduced and when the maximum switching frequency $f_{s\_\max}$ is given, the minimum switching frequency is determined by the range of input voltage. In order to improve the converter efficiency, we should reduce the switching losses and conduction losses. Since the power switches can realize ZCS, the switching losses are quite small and can be ignored compared with conduction losses. Therefore, in order to improve the converter efficiency, we should mainly reduce the conduction losses, which means the circulating current of the resonant tank should be reduced. Since the circulating current of the resonant tank will be reduced with the reduction of the energy that is fed back to the input voltage by the resonant tank. So the optimization goal is to achieve the lowest energy that is fed back to the input voltage by the resonant tank.

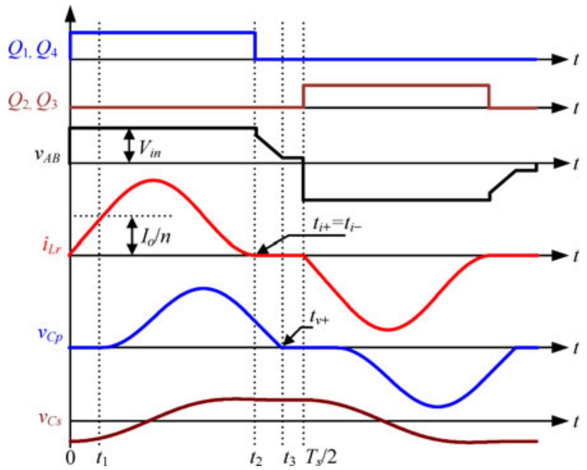

Fig. 5. Key operating waveforms on the boundary of Mode 1 and non-ZCS area (Curve 1 in Fig. 4).

A. *Determine the Optimal Parameters Based on the Mode Boundary Map*

For a generalized design, four normalized parameters, including λ, $I_{o\mathrm{N}}$, $f_{s\mathrm{N}}$ and $V_{o\mathrm{N}}$ are needed to be determined. First, λ and $I_{o\mathrm{N}}$ will be determined based on the mode boundary map.

1) Determine λ and $I_{o\mathrm{N}}$ Based on the Mode Boundary Map: According to Fig. 3, in Mode 1, Mode 2, or Mode 3, when $i_{L_r} < 0$ during $[t_0, T_s/2]$, there is energy fed back to the input voltage. Obviously, the energy that is fed back in Mode 3 is larger than that in Mode 1 and Mode 2, which will result in a low efficiency. In order to achieve a high efficiency, the energy that is fed back to the input voltage should be reduced as small as possible. On the boundary of Mode 1 and non-ZCS area, which is represented by Curve 1 in Fig. 4, the energy that is fed back is zero as shown in Fig. 5, which implies that the converter will achieve the highest efficiency when λ and $I_{o\mathrm{N}}$ are designed on Curve 1.

Since $I_{o\mathrm{N}} = I_o Z_r/(nV_{\mathrm{in}})$, $I_{o\mathrm{N}}$ will decrease (or increase) with the decrease (or increase) of the load current I_o or the increase (or decrease) of the input voltage V_{in}. So from Fig. 4, if λ and $I_{o\mathrm{N}}$ are designed on Curve 1 under arbitrary input voltage and load current conditions, when the input voltage decrease or the load current increase, $I_{o\mathrm{N}}$ will increase and therefore the

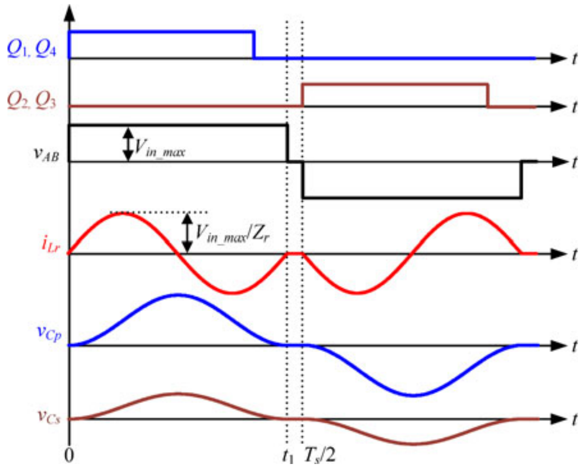

Fig. 6. Key operating waveforms at maximum input voltage and no load.

converter will enter into the non-ZCS region, which will result in the loss of ZCS and thus a reduced efficiency. Therefore, λ and $I_{o\mathrm{N}}$ should be designed on Curve 1 under the condition of minimum input voltage and full load current.

By designing λ and $I_{o\mathrm{N}}$ on Curve 1 under the condition of minimum input voltage and full load current, the resonant tank does not feed energy back to the input. When the input voltage increases or load current decreases, $I_{o\mathrm{N}}$ will decrease and enter into the region below Curve 1, which is shown as the shadow region in Fig. 4. At this time, there is energy fed back to the input. The energy fed back reaches its largest value at maximum input voltage and no load, and in this case, the peak current of i_{L_r} equals to $V_{\mathrm{in\_max}}/Z_r$ as shown in Fig. 6. In order to reduce the energy fed back at maximum input voltage and noload, the characteristic impedance of the resonant tank, Z_r, should be designed to be larger. From Fig. 4, it can be observed that on Curve 1, when λ increases, $I_{o\mathrm{N}}$ will increase. Since $I_{o\mathrm{N}} = I_{o\_\max} Z_r/(nV_{\mathrm{in\_min}})$, Z_r is approximately proportional to $I_{o\mathrm{N}}$. That means if λ is designed larger, Z_r can be designed to be larger. However, if λ is designed to be larger than the value at point *A*, the converter will get into Mode 3 and the efficiency will be degraded. Therefore, λ and $I_{o\mathrm{N}}$ at minimum input voltage and full load current are selected at point *A* is the optimal choice.

2) Determine $f_{s\mathrm{N}}$ and $V_{o\mathrm{N}}$: As discussed above, λ and $I_{o\mathrm{N}}$ at minimum input voltage and full load current should be designed at point *A* to minimize the energy fed back to the input voltage, and thus to improve the converter efficiency. To further improve the converter efficiency, the time interval while $i_{L_r} = 0$ should be reduced, which corresponds to the time interval from t_3 to $T_s/2$, as shown in Fig. 5, since during this time interval, the input voltage does not provide energy to the resonant tank. So it is best to reduce this time interval to zero, and therefore, the converter operates in critical CCM at minimum input voltage and full load current. When the input voltage increases or load current decreases, the converter will enter into DCM. Therefore, $f_{s\mathrm{N}}$ at minimum input voltage and full load should be designed as $f_{s\mathrm{N}} = \pi/(\alpha_1 + \alpha_{12} + \alpha_{23})$, so that the converter operates in critical CCM. When λ, $I_{o\mathrm{N}}$ and $f_{s\mathrm{N}}$ are all determined, $V_{o\mathrm{N}}$ can be determined by (6).

TABLE II
FOUR SETS OF CONVERTER PARAMETERS

Point	λ	$I_{o\mathrm{N}}$	$V_{o\mathrm{N}}$	$f_{s\mathrm{N}}$
A_0	0	1	0.93	0.47
A_1	0.1	1.4	0.91	0.5
A	**0.217**	**2.2**	**0.8**	**0.52**
B	0.25	1.6	0.65	0.42

B. Compare the Set of Parameters at Point A with Other Three Sets of Parameters

To verify that the point *A* is the optimal design point for λ and $I_{o\mathrm{N}}$ at minimum input voltage and full load current, three other points A_0, A_1, and *B* in Fig. 4, are chosen for comparisons. A_0 and A_1 are also on Curve 1. A_0 is a special case as $\lambda = 0$, meaning C_s is so large that it acts as a dc block capacitor and the converter actually performs as a parallel resonant converter. A_1 is a point between A_0 and *A*. Point *B* corresponds to the parameters that designed by [24], which is far away from Curve 1. Table II gives the corresponding λ, $I_{o\mathrm{N}}$, $V_{o\mathrm{N}}$, and $f_{s\mathrm{N}}$ of the points A_0, A_1, *A*, and *B* at minimum input voltage and full load.

Several component stresses of these four points A_0, A_1, *A*, and *B* are selected for comparisons, which include: 1) the rms value of i_{L_r}, denoted by $I_{L_r\_\mathrm{rms}}$, which can reflect the energy feed back of the resonant tank; 2) the peak value of i_{L_r}, denoted by $I_{L_r\_\mathrm{pk}}$, which can reflect the peak current of the power switches; 3) the peak voltage of C_p', denoted by V'_{Cp_pk}, which can reflect the peak voltage of the rectifier diodes. To facilitate calculations, $I_{L_r\_\mathrm{rms}}$, $I_{L_r\_\mathrm{pk}}$ are normalized with respect to $I_{o\_\max}V_o/V_{\mathrm{in\_min}}$, and V'_{Cp_pk} is normalized with respect to V_o, and they are expressed as

$$\begin{cases} I^*_{L_r\_\mathrm{rms}} = \dfrac{I_{L_r\_\mathrm{rms}}}{I_{o\_\max}V_o/V_{\mathrm{in\_min}}} = \dfrac{I_{L_r\mathrm{N\_rms}}}{V_{o\mathrm{N}}I_{o\mathrm{N}}} \\ I^*_{Lr\_\mathrm{pk}} = \dfrac{I_{Lr\_\mathrm{pk}}}{I_{o\_\max}V_o/V_{\mathrm{in\_min}}} = \dfrac{I_{L_r\mathrm{N\_pk}}}{V_{o\mathrm{N}}I_{o\mathrm{N}}} \\ V^*_{C_p\_\mathrm{pk}} = \dfrac{V'_{C_p\_\mathrm{pk}}}{V_o} = \dfrac{V_{C_p\mathrm{N\_pk}}}{V_{o\mathrm{N}}}. \end{cases} \tag{11}$$

According to (6), (8), (9), and (10), $I^*_{L_r\_\mathrm{rms}}$, $I^*_{L_r\_\mathrm{pk}}$, and $V^*_{C_p\_\mathrm{pk}}$ in (11) can be obtained when λ, $I_{o\mathrm{N}}$, and $f_{s\mathrm{N}}$ are given. The curves of $I^*_{L_r\_\mathrm{rms}}$, $I^*_{L_r\_\mathrm{pk}}$, and $V^*_{C_p\_\mathrm{pk}}$ at different load and input voltage are depicted in Figs. 7 and 8. According to Figs. 7(a) and 8(a), $I^*_{L_r\_\mathrm{rms}}$ at *A* is the smallest among A_0, A_1, *A*, and *B* when input voltage and load current changes. According to Figs. 7(b) and 8(b), $I^*_{L_r\_\mathrm{pk}}$ at *A* is also the smallest. According to Figs. 7(c) and 8(c), the maximum value of $V^*_{C_p\_\mathrm{pk}}$ in the variation ranges of input voltage and load current at point *A* is a little higher than that at A_0 and A_1, but lower than that at *B*. Since $I^*_{L_r\_\mathrm{rms}}$ plays a more important role for conduction losses, the point *A* corresponds to the optimal converter parameters. Therefore, these curves in Figs. 7 and 8 have verified the parameters at the point *A* is optimal.

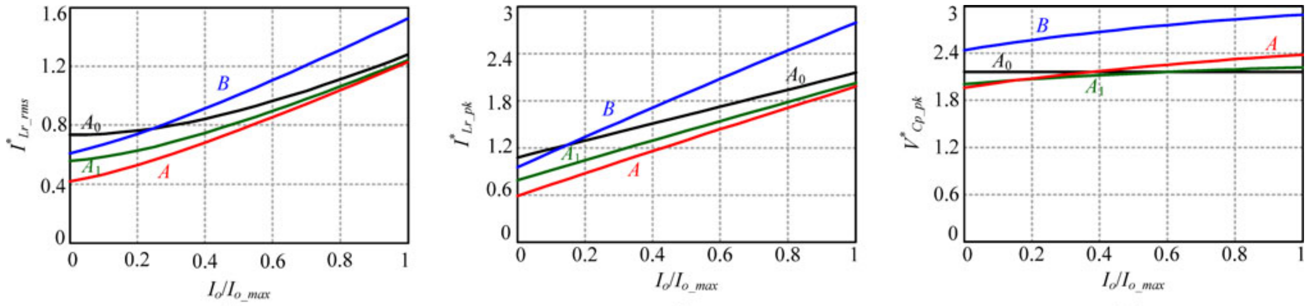

(a) (b) (c)

Fig. 7. Component stresses at different load under minimum input voltage. (a) $I^*_{L_r\_\mathrm{rms}}$. (b) $I^*_{L_r\_\mathrm{pk}}$. (c) $V^*_{C_p\_\mathrm{pk}}$.

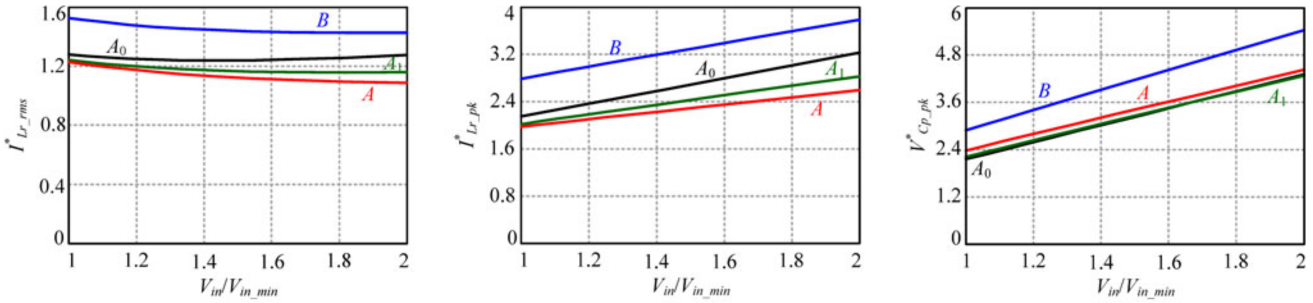

(a) (b) (c)

Fig. 8. Component stresses under different input voltage at full load. (a) $I^*_{L_r\_\mathrm{rms}}$. (b) $I^*_{L_r\_\mathrm{pk}}$. (c) $V^*_{C_p\_\mathrm{pk}}$.

D. Design Procedure

1) Determine the Normalized Parameters According to the Point A with a Certain Margin: While applying the set of parameters of the point *A* in Table II, a certain margin should be kept to prevent the converter from entering non-ZCS area, Mode 3, or CCM. This means λ, $I_{o\mathrm{N}}$, $V_{o\mathrm{N}}$, and $f_{s\mathrm{N}}$ should be a little smaller than that at point *A*.

2) Convert the Normalized Parameters Into Real Values: When the detailed converter specification, which includes the minimum input voltage $V_{\mathrm{in\_min}}$, the full load current I_{o_max}, the output voltage V_o, and the maximum switching frequency f_{s_max} are given, λ, $I_{o\mathrm{N}}$, $V_{o\mathrm{N}}$, and $f_{s\mathrm{N}}$ can be converted into the real converter parameters as

$$\begin{cases} n = \dfrac{V_{o\mathrm{N}} V_{\mathrm{in\_min}}}{V_o} \\ L_r = \dfrac{n V_{\mathrm{in\_min}} I_{o\mathrm{N}} f_{s\mathrm{N}}}{2\pi f_{s\_\mathrm{max}} I_{o\_\mathrm{max}}} \\ C'_p = \dfrac{n\,(1+\lambda)\, I_{o\_\mathrm{max}} f_{s\mathrm{N}}}{8\pi f_{s\_\mathrm{max}} V_{\mathrm{in\_min}} I_{o\mathrm{N}}} \\ C_s = \dfrac{(1+\lambda)\, I_{o\_\mathrm{max}} f_{s\mathrm{N}}}{2\pi\lambda f_{s\_\mathrm{max}} n V_{\mathrm{in\_min}} I_{o\mathrm{N}}}. \end{cases} \tag{12}$$

VI. EXPERIMENTAL RESULTS

Three prototypes of DCM *LCC* resonant converter with inductive filter have been designed with the same specification, where $V_{\mathrm{in\_min}} = 500$ V, $V_{\mathrm{in\_max}} = 600$ V, $V_o = 50$ V, $I_{o\_\mathrm{max}} = 100$ A, and $f_{s\_\mathrm{max}} = 23$ kHz. Prototype 1 is designed with the set of parameters at point *A*. From Table II, to keep a certain margin, we choose $\lambda = 0.21$, $I_{o\mathrm{N}} = 1.7$, $V_{o\mathrm{N}} = 0.7$, and $f_{s\mathrm{N}} = 0.44$. Prototype 2 and prototype 3 are designed with the set of parameters at point *B* and point A_0 for comparison with the prototype 1. For prototype 2, $\lambda = 0.25$, $I_{o\mathrm{N}} = 1.6$, $V_{o\mathrm{N}} = 0.6$, and $f_{s\mathrm{N}} = 0.38$ are chosen to keep a certain margin. For prototype 3, $\lambda = 0.01$, $I_{o\mathrm{N}} = 0.8$, $V_{o\mathrm{N}} = 0.8$, and $f_{s\mathrm{N}} = 0.42$ are chosen to keep a certain margin. From (12), the real converter parameters of these three prototypes are obtained as shown in Table III. For a fair comparison, these three prototypes adopt the same IGBTs (FF50R12RT4 from Infineon), rectifier diodes (DSEI2×101-06A from IXYS), L_f and C_f, where $L_f = 40\ \mu$H and $C_f = 3760\ \mu$F.

TABLE III
PARAMETERS OF THE THREE PROTOTYPES

	L_r	C_s	C'_p	n:1:1
Prototype 1	180 μH	0.30 μF	0.76 μF	7:1:1
Prototype 2	125 μH	0.27 μF	0.60 μF	6:1:1
Prototype 3	90 μH	10 μF	1.5 μF	8:1:1

Figs. 9–11 show the experimental waveforms of the three prototypes at different input voltage and load. From the three figures, the following can be seen:

1) The IGBTs in all the three prototypes all achieve ZCS at different input voltage and load.
2) As seen in Fig. 9(c), parasitic oscillations appear in v_{AB} and i_{L_r}. This is caused by the resonance of L_r and the

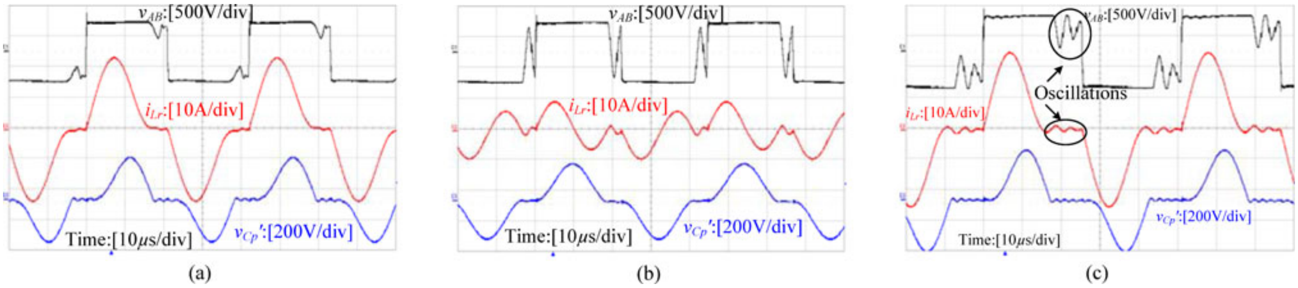

(a) (b) (c)

Fig. 9. Experimental waveforms in prototype 1. (a) $V_{\rm in} = 500$ V, $I_o = 100$ A. (b) $V_{\rm in} = 500$ V, $I_o = 10$ A. (c) $V_{\rm in} = 600$ V, $I_o = 100$ A.

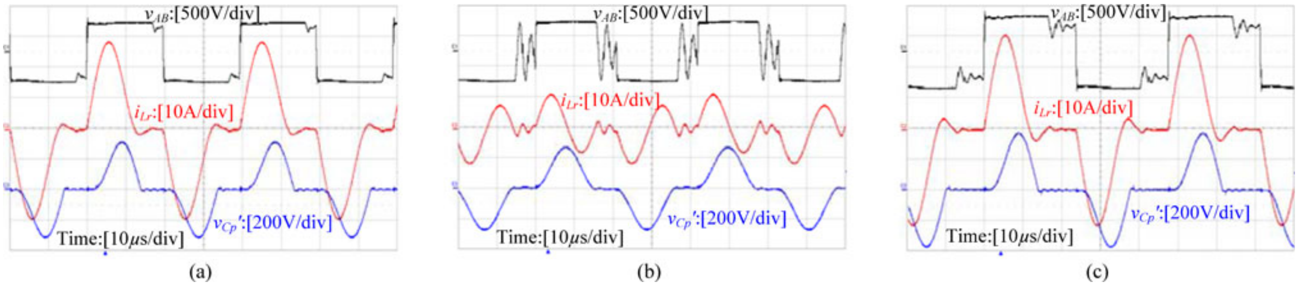

(a) (b) (c)

Fig. 10. Experimental waveforms in prototype 2. (a) $V_{\rm in} = 500$ V, $I_o = 100$ A. (b) $V_{\rm in} = 500$ V, $I_o = 10$ A. (c) $V_{\rm in} = 600$ V, $I_o = 100$ A.

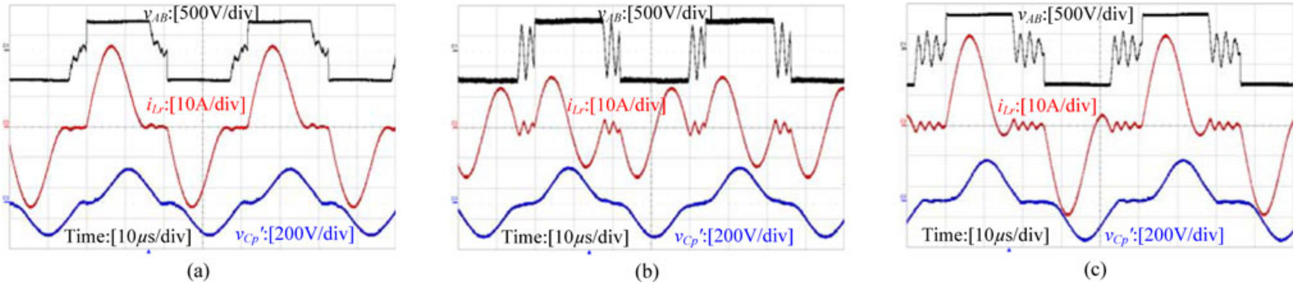

(a) (b) (c)

Fig. 11. Experimental waveforms in prototype 3. (a) $V_{\rm in} = 500$ V, $I_o = 100$ A. (b) $V_{\rm in} = 500$ V, $I_o = 10$ A. (c) $V_{\rm in} = 600$ V, $I_o = 100$ A.

junction capacitors of IGBTs when all the IGBTs are turned off. The energy stored in the junction capacitors of IGBTs is dissipated in the course of the oscillations, which will reduce the converter efficiency. Therefore, it is better to choose the IGBTs, which have small junction capacitors.

3) As seen in Figs. 9(a), 10, (a) and 11(a), when $V_{\rm in} = 500$ V and $I_o = 100$ A, prototype 1 and prototype 3 operate near the boundary of Mode 1 and non-ZCS area, and prototype 2 operates in Mode 2. As seen in Figs. 9(c), 10(c), and 11(c), when $V_{\rm in} = 600$ V and $I_o = 100$ A, prototype 1 and prototype 2 operate in Mode 2, and prototype 3 operates in Mode 1. They are well in agreement with the mode boundary map.

4) The peak value of i_{L_r} in prototype 1 is smaller than that in prototype 2 and prototype 3 with the variations of input voltages and loads. That indicates that prototype 1 can achieve a higher efficiency over the entire input voltage and load range.

Fig. 12(a) shows the measured efficiencies of these three prototypes versus load currents when $V_{\rm in} = 500$ V. Fig. 12(b) shows the measured efficiency of these three prototypes versus input

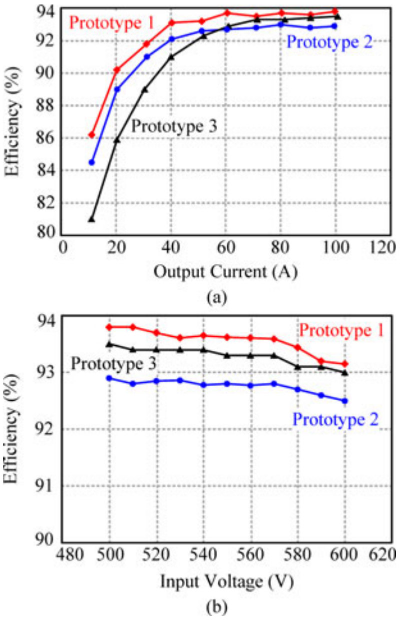

Fig. 12. Efficiency curves (a) versus load at minimum input voltage ($V_{\rm in} =$ 500 V) and (b) versus input voltage at full load ($I_o = 100$ A).

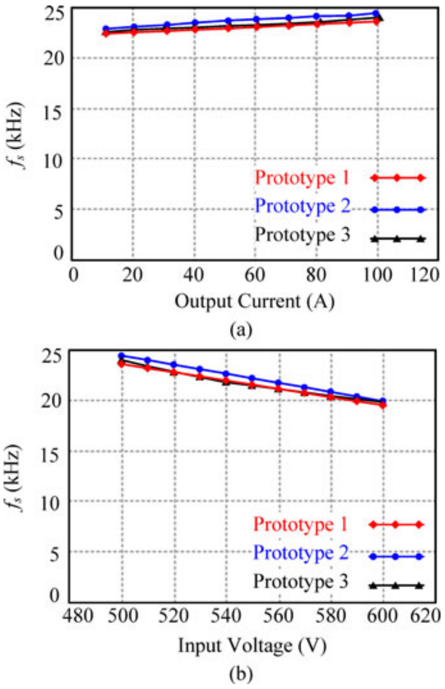

Fig. 13. Switching frequency curves (a) versus load at minimum input voltage ($V_{\rm in} = 500$ V) and (b) versus input voltage at full load ($I_o = 100$ A).

voltages when $I_o = 100$ A. It can be seen that the efficiency of prototype 1 is higher than prototype 2 and prototype 3. It has verified that the set of parameters near point *A* is optimal.

Fig. 13(a) shows the measured switching frequencies of these three prototypes versus load currents when $V_{\rm in} = 500$ V. It can be seen that in any of these three prototypes, the frequency keeps nearly unchanged when the load varies, which verifies the DCM *LCC* resonant converter has a well constant output voltage characteristic. Fig. 13(b) shows the measured switching frequencies of these three prototypes versus input voltages when $I_o = 100$ A. As seen, in any of these three prototypes, the switching frequency is linearly reduced with the increase of input voltage, which is well satisfied with (7).

VII. CONCLUSION

Three main operating modes of DCM *LCC* resonant converter with inductive filter have been reviewed. In order to determine the parameter range of each operating mode, the mode boundary map of the converter has been derived. Based the mode boundary map, a set of optimal and normalized parameters has been found by a generalized optimal design. Several other sets of parameters are compared with the set of optimal parameters by various design curves. Since this set of parameters is normalized, it can be converted into real parameters according to the converter specification. Experiments have verified that with this set of parameters, the converter has a high efficiency over the entire input voltage and load range.

APPENDIX A

A. *Operating Mode 1: Interval 0* [Prior to 0] → *Interval 1* [0, t_1] → *Interval 2* [t_1, t_2] → *Interval 3* [t_2, t_3] → *Interval 0* [$t_3, T_s/2$] [0, t_1]

$$v_{C_s{\rm N}}(\alpha) = 1-(1-V_{C_s{\rm N0}})\cos\left(\sqrt{\frac{\lambda}{1+\lambda}}\alpha\right) \tag{A1}$$

$$v_{C_p{\rm N}}(\alpha) = 0 \tag{A2}$$

$$i_{L_r{\rm N}}(\alpha) = \sqrt{\frac{1+\lambda}{\lambda}}(1-V_{C_s{\rm N0}})\sin\left(\sqrt{\frac{\lambda}{1+\lambda}}\alpha\right). \tag{A3}$$

At t_1, substituting $i_{L_r{\rm N}}(\alpha_1) = I_{o\rm N}$ into (A3) gives

$$\alpha_1 = \sqrt{\frac{1+\lambda}{\lambda}}\arcsin\left(\sqrt{\frac{\lambda}{1+\lambda}}\frac{I_{o\rm N}}{1-V_{C_s{\rm N0}}}\right). \tag{A4}$$

Letting $\alpha = \alpha_1$ and substituting (A4) into (A1) gives

$$V_{C_s{\rm N1}} = 1-\sqrt{(1-V_{C_s{\rm N0}})^2-\frac{\lambda}{1+\lambda}I_{o\rm N}^2}. \tag{A5}$$

[t_1, t_2]

$$\begin{aligned} v_{C_s{\rm N}}(\alpha) = {} & \frac{\lambda}{(1+\lambda)^2}I_{o\rm N}[(\alpha-\alpha_1)+\lambda\sin(\alpha-\alpha_1)] \\ & -\frac{\lambda}{1+\lambda}(1-V_{C_s{\rm N1}})\cos(\alpha-\alpha_1)+\frac{\lambda+V_{C_s{\rm N1}}}{1+\lambda} \end{aligned} \tag{A6}$$

$$\begin{aligned} v_{C_p{\rm N}}(\alpha) = {} & \frac{1-V_{C_s{\rm N1}}}{1+\lambda}[1-\cos(\alpha-\alpha_1)] \\ & +\frac{\lambda I_{o\rm N}}{(1+\lambda)^2}[\sin(\alpha-\alpha_1)-(\alpha-\alpha_1)] \end{aligned} \tag{A7}$$

$$\begin{aligned} i_{L_r{\rm N}}(\alpha) = {} & \frac{I_{o\rm N}}{1+\lambda}[1+\lambda\cos(\alpha-\alpha_1)] \\ & +(1-V_{C_s{\rm N1}})\sin(\alpha-\alpha_1). \end{aligned} \tag{A8}$$

At t_2, substituting $I_{Lr{\rm N2}} = 0$ and $\alpha = \alpha_2$ into (A6)–(A8) gives

$$\begin{aligned} V_{C_s{\rm N2}} = {} & \frac{\lambda I_{o\rm N}}{(1+\lambda)^2}(\alpha_{12}+\lambda\sin\alpha_{12}) \\ & -\frac{\lambda}{1+\lambda}(1-V_{C_s{\rm N1}})\cos\alpha_{12}+\frac{\lambda+V_{C_s{\rm N1}}}{1+\lambda} \end{aligned} \tag{A9}$$

$$\begin{aligned}V_{C_p\mathrm{N}2} = {}& \frac{1 - V_{C_s\mathrm{N}1}}{1+\lambda}\left(1-\cos\alpha_{12}\right)\\ &+\frac{\lambda I_{o\mathrm{N}}}{(1+\lambda)^2}\left(\sin\alpha_{12}-\alpha_{12}\right)\end{aligned} \tag{A10}$$

$$\begin{aligned}0 = {}& \frac{I_{o\mathrm{N}}}{1+\lambda}\left(1+\lambda\cos\alpha_{12}\right)\\ &+\left(1-V_{C_s\mathrm{N}1}\right)\sin\alpha_{12}.\end{aligned} \tag{A11}$$

$[t_2, t_3]$

$$v_{C_s\mathrm{N}}(\alpha) = V_{C_s N2} \tag{A12}$$

$$v_{C_p\mathrm{N}}(\alpha) = V_{C_p\mathrm{N}2} - \frac{I_{o\mathrm{N}}}{1+\lambda}\left(\alpha-\alpha_2\right) \tag{A13}$$

$$i_{L_r\mathrm{N}}(\alpha) = 0. \tag{A14}$$

At t_3, substituting $v_{C_p\mathrm{N}}(\alpha_3) = 0$ into (A13) gives

$$\alpha_{23} = \frac{(1+\lambda)\,V_{C_p\mathrm{N}2}}{I_{o\mathrm{N}}}. \tag{A15}$$

Since the waveform of v_{C_s} is symmetrical in a cycle, we have $v_{C_s}(0) = -v_{C_s}(T_s/2)$. During t_2 to $T_s/2$, v_{C_s} keeps constant, so $v_{C_s}(t_0) = -v_{C_s}(t_2)$. It gives

$$V_{C_s\mathrm{N}2} = -V_{C_s\mathrm{N}0}. \tag{A16}$$

B. Operating Mode 2 and Mode 3: Operating Mode 2 and Mode 3 have the same operating interval sequence and therefore the same equations.

Interval 0 [Prior to t_0]→ *Interval 1* [t_0, t_1]→ *Interval 2* [t_1, t_2] → *Interval 1* [t_2, t_3] → *Interval 0* [t_3, $T_s/2$]

Equations of Mode 2 and Mode 3 before t_2 are the same with Mode 1. At t_2, substituting $\alpha = \alpha_2$ and $V_{C_p\mathrm{N}_2} = 0$ into (A6)–(A8) gives

$$\begin{aligned}V_{C_s\mathrm{N}2} = {}& \frac{\lambda I_{o\mathrm{N}}}{(1+\lambda)^2}\left(\alpha_{12}+\lambda\sin\alpha_{12}\right)\\ &-\frac{\lambda}{1+\lambda}\left(1-V_{C_s\mathrm{N}1}\right)\cos\alpha_{12}+\frac{\lambda+V_{C_s\mathrm{N}1}}{1+\lambda}\end{aligned} \tag{A17}$$

$$\left(1-V_{C_s\mathrm{N}1}\right)\left(1-\cos\alpha_{12}\right)+\frac{\lambda I_{o\mathrm{N}}}{1+\lambda}\left(\sin\alpha_{12}-\alpha_{12}\right) = 0 \tag{A18}$$

$$I_{L_r\mathrm{N}2} = \frac{I_{o\mathrm{N}}}{1+\lambda}\left(1+\lambda\cos\alpha_{12}\right)+\left(1-V_{C_s\mathrm{N}1}\right)\sin\alpha_{12}. \tag{A19}$$

$[t_2, t_3]$

$$\begin{aligned}v_{C_s\mathrm{N}}(\alpha) = {}& 1-\left(1-V_{C_s\mathrm{N}2}\right)\cos\left[\sqrt{\frac{\lambda}{1+\lambda}}\left(\alpha-\alpha_2\right)\right]\\ &+\sqrt{\frac{\lambda}{1+\lambda}}I_{L_r\mathrm{N}2}\sin\left[\sqrt{\frac{\lambda}{1+\lambda}}\left(\alpha-\alpha_2\right)\right]\end{aligned} \tag{A20}$$

$$v_{C_p\mathrm{N}}(\alpha) = 0 \tag{A21}$$

$$\begin{aligned}i_{L_r\mathrm{N}}(\alpha) = {}& I_{L_r\mathrm{N}2}\cos\left[\sqrt{\frac{\lambda}{1+\lambda}}\left(\alpha-\alpha_2\right)\right]\\ &+\sqrt{\frac{1+\lambda}{\lambda}}\left(1-V_{C_s\mathrm{N}2}\right)\sin\left[\sqrt{\frac{\lambda}{1+\lambda}}\left(\alpha-\alpha_2\right)\right].\end{aligned} \tag{A22}$$

At t_3, substituting $\alpha = \alpha_3$ into (A20) and (A22) and letting $i_{L_r\mathrm{N}}(\alpha_3) = 0$ gives

$$\begin{aligned}V_{C_s\mathrm{N}3} = {}& 1-\left(1-V_{C_s\mathrm{N}2}\right)\cos\left[\sqrt{\frac{\lambda}{1+\lambda}}\alpha_{23}\right]\\ &+\sqrt{\frac{\lambda}{1+\lambda}}I_{L_r\mathrm{N}2}\sin\left[\sqrt{\frac{\lambda}{1+\lambda}}\alpha_{23}\right]\end{aligned} \tag{A23}$$

$$\begin{aligned}0 = {}& I_{L_r\mathrm{N}2}\cos\left[\sqrt{\frac{\lambda}{1+\lambda}}\alpha_{23}\right]\\ &+\sqrt{\frac{1+\lambda}{\lambda}}\left(1-V_{C_s\mathrm{N}2}\right)\sin\left[\sqrt{\frac{\lambda}{1+\lambda}}\alpha_{23}\right].\end{aligned} \tag{A24}$$

Once again, the waveform of v_{C_s} is symmetrical in a cycle, we have $v_{C_s}(0) = -v_{C_s}(T_s/2)$. During t_3 to $T_s/2$, v_{C_s} keeps constant, so $v_{C_s}(0) = -v_{C_s}(t_3)$. It gives

$$V_{C_s\mathrm{N}3} = -V_{C_s\mathrm{N}0}. \tag{A25}$$

APPENDIX B

The derivation of (3), which is the equation of the boundary curve between Mode 1 and non-ZCS area, is shown as follows.

Since there are six unknown quantities, which are λ, $I_{o\mathrm{N}}$, $V_{C_s\mathrm{N}1}$, $V_{C_s\mathrm{N}0}$, $V_{C_s\mathrm{N}2}$, and α_{12} in the following five equations: (2), (A5), (A9), (A11), and (A16), by elimination method, $V_{C_s\mathrm{N}1}$, $V_{C_s\mathrm{N}0}$, $V_{C_s\mathrm{N}2}$, and α_{12} can be eliminated and (3) can be obtained.

First, substituting (A16) into (A9) gives

$$\begin{aligned}-V_{C_s\mathrm{N}0} = {}& \frac{\lambda I_{o\mathrm{N}}}{(1+\lambda)^2}\left(\alpha_{12}+\lambda\sin\alpha_{12}\right)\\ &-\frac{\lambda}{1+\lambda}\left(1-V_{C_s\mathrm{N}1}\right)\cos\alpha_{12}+\frac{\lambda+V_{C_s\mathrm{N}1}}{1+\lambda}.\end{aligned} \tag{B1}$$

Substituting (A5) into (B1), (2), and (A11), we can obtain (B2), (B3), and (B4), respectively

$$\begin{aligned}-V_{C_s\mathrm{N}0} = {}& \frac{\lambda I_{o\mathrm{N}}}{(1+\lambda)^2}\left(\alpha_{12}+\lambda\sin\alpha_{12}\right)\\ &-\frac{\lambda}{1+\lambda}\sqrt{\left(1-V_{C_s\mathrm{N}0}\right)^2-\frac{\lambda}{1+\lambda}I_{o\mathrm{N}}^2}\cos\alpha_{12}\\ &+1-\frac{1}{1+\lambda}\sqrt{\left(1-V_{C_s\mathrm{N}0}\right)^2-\frac{\lambda}{1+\lambda}I_{o\mathrm{N}}^2}\end{aligned} \tag{B2}$$

$$V_{C_s\mathrm{N}0} = 1 - \frac{1}{\sqrt{1+\lambda}} I_{o\mathrm{N}} \tag{B3}$$

$$0 = \frac{I_{o\mathrm{N}}}{1+\lambda}\left(1+\lambda\cos\alpha_{12}\right) + \sqrt{\left(1-V_{C_s\mathrm{N}0}\right)^2 - \frac{\lambda}{1+\lambda} I_{o\mathrm{N}}^2}\,\sin\alpha_{12}. \tag{B4}$$

Substituting (B3) into (B2) and (B4), we can obtain (B5) and (B6), respectively

$$0 = \frac{\lambda I_{o\mathrm{N}}}{(1+\lambda)^2}\left(\alpha_{12}+\lambda\sin\alpha_{12}\right) - \frac{\lambda}{1+\lambda}\sqrt{\frac{1-\lambda}{1+\lambda}} I_{o\mathrm{N}}\cos\alpha_{12} + 2 - \frac{1}{1+\lambda}\sqrt{\frac{1-\lambda}{1+\lambda}} I_{o\mathrm{N}} - \frac{1}{\sqrt{1+\lambda}} I_{o\mathrm{N}} \tag{B5}$$

$$\alpha_{12} = 1.5\pi - \arcsin(\lambda). \tag{B6}$$

Substituting (B6) into (B5), we can obtain (3).

APPENDIX C

The derivation of the approximate expression of the voltage gain in Mode 1 and Mode 2 is as follows.

Since the average input power and output power during [0, $T_s/2$] are equal, we have

$$V_{\mathrm{in}}\frac{2}{T_s}\int_{t_0}^{T_s/2} i_{Lr}(t)dt = V_o I_o. \tag{C1}$$

According to Fig. 3(a) and (b), in Mode 1 and Mode 2, i_{L_r} can be approximated to the sum of a dc component and a sinusoidal component in the course of resonance. Since most of the energy that is transferred from input to output is during $[t_1, t_2]$ in half cycle, according to (A8), the approximate expression of i_{L_r} in half cycle can be written as

$$i_{Lr}(t) = \begin{cases} \dfrac{I_o}{n(1+\lambda)} + I_{L_r m}\sin(\omega_r t), & 0 \le t \le T_r \\ 0, T_r \le t \le T_s/2 \end{cases} \tag{C2}$$

where $I_{L_r m}$ represents the amplitude of the sinusoidal component of i_{L_r}.

Substituting (C2) into (C1), we have

$$\frac{nV_o}{V_{\mathrm{in}}} = \frac{2}{T_s}\frac{T_r}{(1+\lambda)}. \tag{C3}$$

According to Table I, the normalized form of (C3) can be obtained, which is (7). Although the aforementioned derivation process of the approximate expression of voltage gain (7) is not very strict, a lot of the checking calculations have testified that (7) is with sufficient accuracy. Especially in the shadow region of Fig. 4, the margin of error of (7) is no bigger than 2%.

REFERENCES

[1] L. Sun, J. He, Y. Pei, and Z. Wang, "Design and optimization of high current intelligent waveform power supply for electroplating," in *Proc. IEEE Power Electron. Motion Control Conf.*, 2012, pp. 1516–1521.

[2] I. D. Kim, W. W. Cho, J. Y. Kim, and E. C. Nho, "Design of low-voltage high-current rectifier with high-efficiency output side for electrolytic disinfection of ballast water," in *Proc. IEEE Energy Convers. Congr. Expo.*, 2010, pp. 1652–1657.

[3] N. Frohleke, H. Mundinger, S. Beineke, P. Wallmeier, and H. Grotstollen, "Resonant transition switching welding power supply," in *Proc. IEEE Ind. Electron., Control Instrum.*, 1997, pp. 615–620.

[4] E. J. Dede, G. Garcera, V. Esteve, J. M. Benavent, J. A. Carrasco, and A. Ferreres, "On the design of a high current power supply for superconducting magnet," in *Proc. IEEE Power Electron. Spec. Conf.*, 1996, pp. 894–897.

[5] G. Ivensky, I. Zeltser, A. Kats, and S. Ben-Yaakov, "Reducing IGBT losses in ZCS series resonant converters," *IEEE Trans. Ind. Electron.*, vol. 46, no. 1, pp. 67–74, Feb. 1999.

[6] Y. Lo, C. Lin, M. Hsieh, and C. Lin, "Phase-shifted full-bridge series-resonant DC–DC converter for wide load variations," *IEEE Trans. Ind. Electron.*, vol. 58, no. 6, pp. 2572–2575, Jun. 2011.

[7] H. Sheng, W. Shen, H. Wang, D. Fu, Y. Pei, X. Yang, F. Wang, D. Boroyevich, F. C. Lee, and C. W. Tipton, "Design and implementation of a high power density three-level parallel resonant converter for capacitor charging pulsed-power supply," *IEEE Trans. Plasma Sci.*, vol. 39, no. 4, pp. 1131–1140, Apr. 2011.

[8] R. L. Steigerwald, "A comparison of half-bridge resonant converter topologies," *IEEE Trans. Power Electron.*, vol. 3, no. 2, pp. 174–182, Apr. 1988.

[9] R. P. Severns, "Topologies for three-element resonant converter," *IEEE Trans. Power Electron.*, vol. 7, no. 1, pp. 89–98, Jan. 1992.

[10] I. Batarseh, "Resonant converter topologies with three and four energy storage elements," *IEEE Trans. Power Electron.*, vol. 9, no. 1, pp. 64–73, Jan. 1994.

[11] B. Yang, F. C. Lee, A. J. Zhang, and G. Huang, "LLC resonant converter for front end DC/DC conversion," in *Proc. IEEE Appl. Power Electron. Conf. Expo.*, 2002, pp. 1108–1112.

[12] W. Feng and F. C. Lee, "Optimal trajectory control of LLC resonant converter for soft start-up," *IEEE Trans. Power Electron.*, vol. 29, no. 3, pp. 1461–1468, Mar. 2014.

[13] A. J. Gilbert, C. M. Bingham, D. A. Stone, and M. P. Foster, "Normalized analysis and design of *LCC* resonant converters," *IEEE Trans. Power Electron.*, vol. 22, no. 6, pp. 2386–2402, Nov. 2007.

[14] D. Fu, F. C. Lee, Q. Yang, and F. Wang, "A novel high-power-density three-level *LCC* resonant converter with constant-power-factor-control for charging applications," *IEEE Trans. Power Electron.*, vol. 23, no. 5, pp. 2411–2420, Sep. 2008.

[15] J. Liu, L. Sheng, J. Shi, Z. Zhang, and X. He, "*LCC* resonant converter operating in discontinuous resonant current mode in high voltage, high power and high frequency applications," in *Proc. IEEE Appl. Power Electron. Conf. Expo.*, 2009, pp. 1482–1486.

[16] J. Biela, U. Badstuebner, and J. W. Kolar, "Design of a 5-kW, 1-U, 10-kW/dm3 resonant DC–DC converter for telecom applications," *IEEE Trans. Power Electron.*, vol. 24, no. 7, pp. 1701–1710, Jul. 2009.

[17] T. Soeiro, J. Muhlethaler, J. Linner, P. Ranstad, and J. Kolar, "Automated design of a high power high frequency *LCC* resonant converter for electrostatic precipitators," *IEEE Trans. Ind. Electron.*, vol. 60, no. 11, pp. 4805–4819, Nov. 2013.

[18] G. Ivensky, A. Kats, and S. Ben-Yaakov, "An RC load model of parallel and series-parallel resonant DC–DC converters with capacitive output filter," *IEEE Trans. Power Electron.*, vol. 14, no. 3, pp. 515–521, May 1999.

[19] R. Yang, H. Ding, Y. Xu, L. Yao, and Y. Xiang, "An analytical steady-state model of *LCC* type series-parallel resonant converter with capacitive output filter," *IEEE Trans. Power Electron.*, vol. 29, no. 1, pp. 328–338, Jan. 2014.

[20] A. J. Forsyth, G. A. Ward, and S. V. Mollov, "Extended fundamental frequency analysis of the *LCC* resonant converter," *IEEE Trans. Power Electron.*, vol. 18, no. 6, pp. 1286–1292, Nov. 2003.

[21] A. K. S. Bhat, "Analysis and design of a series–parallel resonant converter," *IEEE Trans. Power Electron.*, vol. 8, no. 1, pp. 1–11, Jan. 1993.

[22] A. K. S. Bhat, "Analysis and design of a high-frequency resonant converter using *LCC*-type commutation," *IEEE Trans. Power Electron.*, vol. 2, no. 4, pp. 291–301, Oct. 1987.

[23] S. Shah and A. K. Upadhyay, "Analysis and design of a half-bridge series-parallel resonant converter operating in discontinuous conduction mode," in *Proc. IEEE Appl. Power Electron. Conf. Expo.*, 1990, pp. 165–174.

[24] V. Belaguli and A. K. S. Bhat, "Series-parallel resonant converter operating in discontinuous current mode-analysis, design, simulation, and experimental results," *IEEE Trans. Circuits Syst.*, vol. 47, no. 4, pp. 433–442, Apr. 2000.

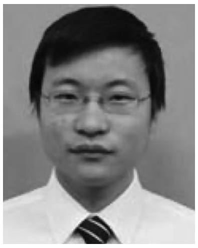

Xing Tan (S'2013) was born in Hubei Province, China, in 1987. He received the B.S. degree in electrical and electronic engineering, in 2009, from the Huazhong University of Science and Technology, Wuhan, China, where he is currently working toward the Ph.D. degree.

His current research interests include soft-switching dc–dc converters and resonant converters.

Xinbo Ruan (M'97–SM'02) was born in Hubei Province, China, in 1970. He received the B.S. and Ph.D. degrees in electrical engineering from the Nanjing University of Aeronautics and Astronautics (NUAA), Nanjing, China, in 1991 and 1996, respectively.

In 1996, he joined the Faculty of Electrical Engineering Teaching and Research Division, NUAA, where he became a Professor in the College of Automation Engineering in 2002 and has been engaged in teaching and research in the field of power electronics. From August to October 2007, he was a Research Fellow in the Department of Electronic and Information Engineering, Hong Kong Polytechnic University, Hong Kong, China. Since March 2008, he has been also with the School of Electrical and Electronic Engineering, Huazhong University of Science and Technology, Wuhan, China. He is a Guest Professor with Beijing Jiaotong University, Beijing, China; Hefei University of Technology, Hefei, China; and Wuhan University, Wuhan, China. He is an author or coauthor of five books and more than 180 technical papers published in journals and conferences. His current research interests include soft-switching dc–dc converters, soft-switching inverters, power factor correction converters, modeling the converters, power electronics system integration, and renewable energy generation system.

Dr. Ruan was a recipient of the Delta Scholarship by the Delta Environment and Education Fund in 2003 and was a recipient of the Special Appointed Professor of the Chang Jiang Scholars Program by the Ministry of Education, China, in 2007. From 2005 to 2013, he was the Vice President of the China Power Supply Society, and since 2008, he has been a member of the Technical Committee on Renewable Energy Systems within the IEEE Industrial Electronics Society. He has been an Associate Editor for the IEEE TRANSACTIONS ON INDUSTRIAL ELECTRONICS and the IEEE JOURNAL OF EMERGING AND SELECTED TOPICS ON POWER ELECTRONICS since 2011 and 2013, respectively. He is a Senior Member of the IEEE Power Electronics Society and the IEEE Industrial Electronics Society.